The Astrophysical Journal, 680:474–482, 2008 June 10

CONSTRAINING THE EARLIEST CIRCUMSTELLAR DISKS AND THEIR ENVELOPES

Hsin-Fang Chiang,[1] Leslie W. Looney,[1] Konstantinos Tassis,[2] Lee G. Mundy,[3] and Telemachos Ch. Mouschovias[4]

Received 2007 November 26; accepted 2008 March 7

ABSTRACT

Using interferometric data from BIMA observations, combined with detailed modeling in Fourier space of the physical structures predicted by models, we constrain the circumstellar envelope parameters for four Class 0 young stellar objects, as well as their embedded circumstellar disks. The envelopes of these objects are still undergoing collapse, and theoretical collapse models can be compared to the observations. Since it has been suggested in a previous study that both the Larson-Penston and Shu similarity solutions underestimate the age of the system, we adopt Tassis & Mouschovias' model of the collapse process, which includes all relevant magnetic fields effects. The results of the model fitting show a good consistency between theory and data; furthermore, no age problem exists, since the Tassis & Mouschovias' model is age independent for the first 255 kyr. Although the majority of the continuum dust emission arises from the circumstellar envelopes, these objects have well-known outflows, which suggest the presence of circumstellar disks. At the highest resolution, most of the large-scale envelope emission is resolved out by interferometry, but the small-scale residual emission remains, making it difficult to observe only the compact disk component. By modeling the emission of the envelope and subtracting it from the total emission, we constrain the disk masses in our four systems to be comparable to or smaller than the typical disk masses for T Tauri systems.

Subject headings: circumstellar matter — magnetic fields — radio continuum: stars — stars: formation — stars: pre–main-sequence — techniques: interferometric

1. INTRODUCTION

The standard scenario of low-mass star formation starts at the collapse of prestellar cores and the formation of central protostellar objects. These young stellar objects (YSOs) evolve through the so-called Class 0, I, II, and III stages, which are thought to be a temporal sequence (e.g., Lada & Wilking 1984; Adams et al. 1987; Andre et al. 1993, 2000). In the earliest stage, i.e., Class 0 stage, when the central YSO is just forming inside the surrounding envelope (of mass ≈a few solar masses; e.g., Looney et al. 2000, hereafter LMW00), the envelope is still undergoing gravitational collapse onto the circumstellar disk. The YSO powers the bipolar outflows, which carve away the polar region of the envelope by entraining envelope material and widening their opening angles (e.g., Bachiller 1996; Arce & Sargent 2006; Seale & Looney 2008). At this early time, the envelope mass is >85% of the system mass (Looney et al. 2003, hereafter LMW03). As the system evolves, the envelope loses mass as material is transported down through the circumstellar disk onto the protostars or carried away with the outflows. Eventually, the YSO circumstellar structure is dominated by the disk (a hundredth of a solar mass; e.g., Andrews & Williams 2005). The circumstellar disk evolves, presumably becoming a planetary system like the solar system.

The initial collapse process of low-mass protostars is often described by self-similar isothermal solutions, which are a continuum of solutions (e.g., Whitworth & Summers 1985) that range from the "inside-out" collapse solution (Shu 1977; hereafter the Shu solution) to the Larson-Penston solution (Larson 1969; Penston 1969; Hunter 1977; hereafter the LP solution). These models generally obtain an inner core with a power-law density profile $\rho \propto r^{-3/2}$ that increases in radius with time, surrounded by a $\rho \propto r^{-2}$ envelope. The theoretical density profiles from these solutions have been compared to observations of the dust continuum emission (e.g., LMW03; Harvey et al. 2003; Jørgensen et al. 2005), but the models cannot fit the observations with reasonable physical parameters (required age is too low; see LMW03), which consequently hints at the need for more sophisticated theoretical models that include more of the essential physical processes of the collapse mechanisms, for example, turbulence and/or magnetic fields.

The theory of turbulence-induced star formation postulates that turbulence causes overdensities and is thus responsible for the core formation in molecular clouds, while magnetic fields are not dynamically important and do not have a significant impact on this process (see reviews of Mac Low & Klessen 2004; Elmegreen & Scalo 2004). At this time, there are no predictions of the density of a protostellar object that is produced by turbulence-induced collapse. Moreover, the nonthermal contribution of the observed line widths is small in evolved, collapsing molecular cloud cores (e.g., Benson & Myers 1989; Barranco & Goodman 1998; Kirk et al. 2007). Whether turbulence plays an important role in the formation and evolution of protostellar fragments (or cores) is still under debate. On the other hand, the theory of ambipolar-diffusion-initiated star formation predicts the formation of thermally and magnetically supercritical protostellar cores inside magnetically subcritical parent clouds (see reviews of Mouschovias 1996; Mouschovias & Ciolek 1999). In the framework of the ambipolar-diffusion-induced collapse, there are extensive studies of the dynamics of the prestellar phase (e.g., Tassis & Mouschovias 2007a, 2007b, 2007c) and the accretion process after a protostar has formed at the center of the core (Tassis & Mouschovias 2005a, 2005b, hereafter TM05), which can be compared to observations.

TM05 have constructed a six-fluid MHD simulation to study the accretion process of matter from a molecular cloud core onto a protostellar object in the presence of magnetic fields. In their model, they track the evolution of magnetic flux and six kinds of

---

[1] Department of Astronomy, University of Illinois at Urbana-Champaign, 1002 West Green Street, Urbana, IL 61801; hchiang2@uiuc.edu.

[2] Department of Astronomy and Astrophysics and the Kavli Institute for Cosmological Physics, University of Chicago, Chicago, IL 60637.

[3] Department of Astronomy, University of Maryland, College Park, MD 20742.

[4] Departments of Physics and Astronomy, University of Illinois at Urbana-Champaign, 1002 West Green Street, Urbana, IL 61801.

particles (neutral molecules, atomic and molecular ions, electrons, neutral grains, negatively charged grains, and positively charged grains, among which only the electrons are assumed to be attached to the magnetic field lines) in a self-gravitating, accreting molecular cloud core. The simulation starts with a magnetically supported parent cloud. Ambipolar diffusion leads to the formation of a thermally and magnetically supercritical core that begins to contract dynamically. Its innermost part reaches nearly hydrostatic equilibrium while its outer part still undergoes infall. At the moment when the hydrostatic protostellar core has just formed at the center (called $t = 0$), the inner core region including the protostar is replaced by a central sink to facilitate the calculation. As time progresses and mass and magnetic flux accrete onto the protostar from the envelope, a region of enhanced magnetic field, called the "magnetic wall," forms and drives an outward-propagating shock. Behind the shock, gravity dominates over the magnetic forces and reaccelerates the neutral particles, which continue to accrete onto the protostar until the next magnetic wall is formed. The magnetic wall forms and disperses in a quasi-periodic manner. Because of the presence of the magnetically controlled bursts, accretion from the envelope onto the protostar is episodic over the first 255 kyr.

Interferometric data of Class 0 objects provide the best means to test these theories. One of the features of an interferometer is the ability to spatially filter emission. Indeed, dust continuum observations of young protostars have often been used to peer inside the bright envelope to reveal the young, compact circumstellar disk (e.g., Keene & Masson 1990). Dust continuum emission is often used, but molecular lines can also be excellent tracers of specific conditions. However, using molecular lines to trace the disks does present some difficulties in the case of the youngest stars: (1) active accretion and outflow processes at multiple scales, (2) chemistry effects and evolution, and (3) shocks in the outflow, the disk, and the disk/envelope interface region. All of these contaminate the preferred disk-only tracers and make it difficult to disentangle any molecular result without a good understanding of the envelope structure derived from the dust continuum modeling (e.g., Brinch et al. 2007).

Regardless of the tracers used, more intricate theoretical models than the "inside-out" collapse can be tested observationally. In this paper, we build on the observational data of LMW00: $\lambda =$ 2.7 mm dust continuum images of 24 young stellar sources with sensitivity to spatial scales from $0.5''$ to $50''$. A discussion of the data acquisition and images can be found in that paper. We follow the work of LMW03, which presented modeling of the envelope emission of Class 0 objects, and use the four sources from that work with the highest signal-to-noise ratio (NGC 1333 IRAS 4A, NGC 1333 IRAS 4B, NGC 1333 IRAS 2A, and L1448 IRS 3B). We compare the predicted density profiles from TM05 to these data and comment on the results with respect to those found in LMW03.

2. SOURCES

All four sources modeled in this study are in the Perseus molecular cloud, a low-mass star forming region probably in the vicinity of the massive star forming region Per OB2 association. Dense cores and YSO candidates at all evolutionary stages (Class 0, I, II, and III) have been found in Perseus via radio and infrared observations. IC 348 and NGC 1333 are the two main dense clusters, and other smaller groups like L1448, L1455, Barnard 1, and Barnard 5 are also associated with many low-mass protostars (e.g., Enoch et al. 2006; Jørgensen et al. 2006). The exact distance to the Perseus molecular cloud is still uncertain and ranges from 220 to 350 pc. The smaller value is based on the distance–interstellar extinction relation using photometry (Cernis 1990); the distance may be the larger value if the Perseus molecular cloud is physically related to the Per OB2 association, *Hipparcos* parallax distance of 318 ± 27 pc (de Zeeuw et al. 1999). Since Perseus is composed of a long chain of dense clouds with a total length of about 30 pc, there may be a distance gradient, or it may be composed of several layers of clouds. Cernis (1993) showed a distance difference from the eastern part ($\sim$260 pc) to the western part ($\sim$220 pc). In this study, we adopt a distance of 350 pc for NGC 1333 and 300 pc for L1448, as in LMW03, to facilitate comparison. Since we are using roughly the upper limit of the distance, this assumption may lead to overestimates of the envelope and disk masses and underestimates of the source size.

2.1. *NGC 1333 IRAS 4*

NGC 1333 is a reflection nebula with mainly two embedded protostellar clusters in the L1450 dark nebula in the Perseus molecular cloud. The age of the young cluster is about 1 Myr, estimated by the fraction of infrared excess sources and a *K*-band luminosity function comparison (Lada et al. 1996), consistent with the age estimated by brown dwarf studies (e.g., Wilking et al. 2004). The plentiful jet and outflow activities driven by YSOs in this region also imply that it is an active star-forming region at an early stage of evolution (e.g., Bally et al. 1996; Knee & Sandell 2000).

The multiple system NGC 1333 IRAS 4 (hereafter just IRAS 4) contains three main groups of sources, designated as 4A, 4B, and 4C (Sandell & Knee 2001). The brightest Class 0 component IRAS 4A has been detected as a binary system separated by $1.8''$ with a common circumbinary envelope (Lay et al. 1995; LMW00) A highly collimated N-S molecular outflow driven by IRAS 4A2 has been observed with estimated dynamical age of about 6000 yr (Blake et al. 1995; Choi 2005). A dimmer southern outflow probably driven by 4A1 has been mapped in HCN and SiO, but no northern counterpart has been detected (Choi 2001, 2005). SMA polarimetric observations have shown the magnetic field geometry of IRAS 4A and supported the magnetic theory of star formation (Girart et al. 2006).

IRAS 4B is a binary system with a separation of $\sim 10''$ between 4BW and 4BE (Sandell & Knee 2001); 4BE is also named as 4B', 4BII, or 4C in different references. Note that 4C is mostly used as the name of another millimeter object $\sim 50''$ northeast of 4A. A compact collimated outflow driven by IRAS 4BW has been observed (e.g., Choi 2001; Di Francesco et al. 2001) and shown a short dynamical timescale.

2.2. *NGC 1333 IRAS 2A*

NGC 1333 IRAS 2 (hereafter IRAS 2) has been resolved into three sources (Sandell & Knee 2001), including two Class 0 protostars, IRAS 2A and IRAS 2B, and a starless core, IRAS 2C (Jørgensen et al. 2004). Two CO outflows have been mapped, one in the NNE-SSW direction and the other in the E-W direction (e.g., Knee & Sandell 2000). Since these two outflows are orthogonal to each other and have quite different properties, they may have different driving sources. The E-W outflow may be driven by IRAS 2A, while the NNE-SSW outflow may be driven by IRAS 2C (Knee & Sandell 2000). It is also possible that both are driven by IRAS 2A, which may be an unresolved binary. IRAS 2B may drive the third outflow in this region, but only the blueshifted lobe has been identified (Knee & Sandell 2000).

2.3. *L1448 IRS 3B*

The star forming region L1448 is located $\sim 1^\circ$ southwest of NGC 1333 in Perseus and contains many YSOs: Class I source

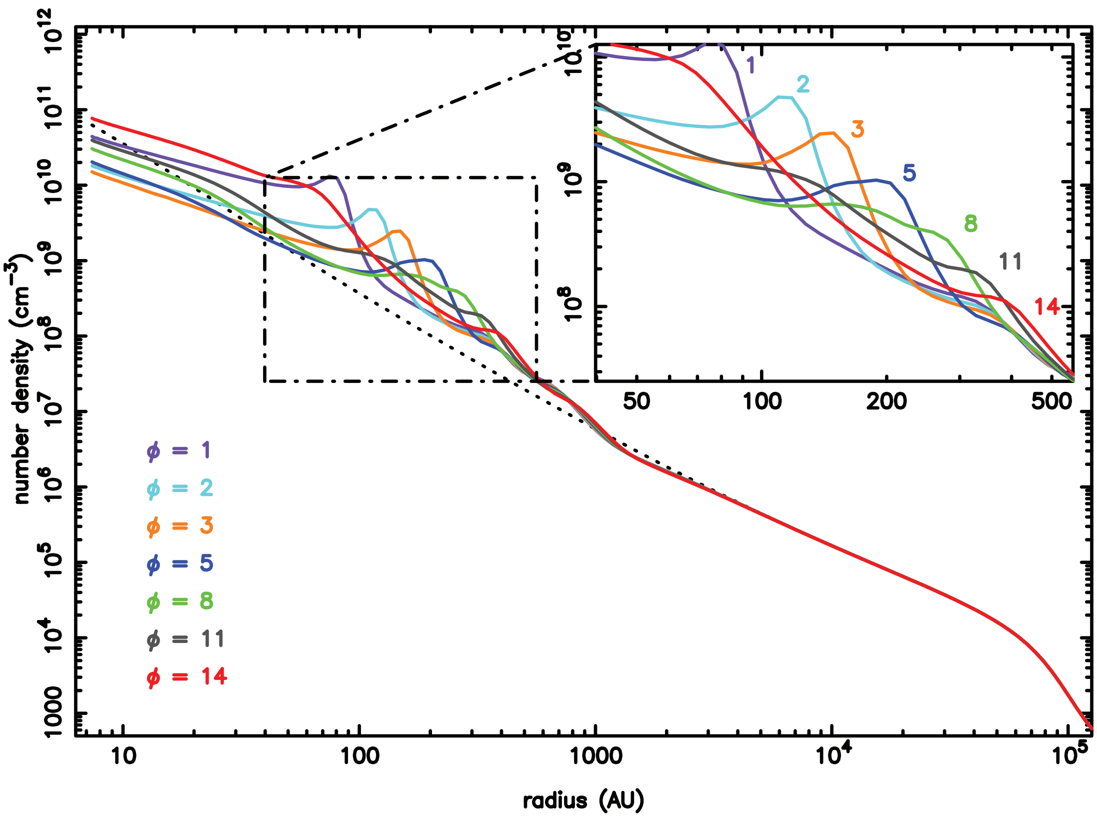

Fig. 1.—Number density profiles of neutral particles in a typical magnetic cycle at different phases from the TM05 model. These curves show phases 1, 2, 3, 5, 8, 11, and 14, which correspond to $t = 33750$, 34000, 34250, 34750, 35500, 36250, and 37000 yr after formation of the central protostar. The shock driven by the "magnetic wall" forms, propagates outward, and disperses throughout a cycle. Although this is a particular cycle, no obvious differences are found between cycles, that is, every magnetic cycle goes through similar phases, except that the period of the cycle varies as the system evolves (see TM05a, TM05b for more details).

L1448 IRS 1, Class 0 sources L1448 IRS 2, L1448 IRS 3 (also known as L1448 N), and L1448-mm (also know as L1448 C) are the most well known (e.g., Jørgensen et al. 2006; O'Linger et al. 2006). Many of these YSOs have been resolved into binary systems; for example, L1448 IRS 3 and L1448-mm are both binary systems. Multiple outflows have been found in this region. The huge molecular outflows emanating from L1448-mm and L1448 IRS 2 are almost parallel to each other, and some of them even have multiple overlapping components (e.g., Wolf-Chase et al. 2000; Kwon et al. 2006; Tobin et al. 2007).

L1448 IRS 3 is composed of three sources, among which IRS 3A (L1448 N:A) and IRS 3B (L1448 N:B) are separated by $7''$ and have a common envelope in a protobinary system, and IRS 3C (L1448 NW) is $20''$ northwest of them (LMW00). All of them are Class 0 objects, except that IRS 3A is slightly closer to the transition between Class 0 and Class I (O'Linger et al. 2006). Two interacting outflows driven by IRS 3A and IRS 3B, respectively, have been studied by Kwon et al. (2006).

3. MODELING

To compare the theoretical models of TM05 and the LMW00 observations, we characterize the observed dust continuum emission, which depends on the dust density, grain properties, and temperature.

3.1. *Density Profiles*

In the theoretical TM05 model, the physical parameters of the envelope are shown to have a quasi-periodic variation beginning at a time about 15 kyr after the formation of a hydrostatic protostellar core. The density goes through a cycle profile that is largely invariant with time from 15 to 255 kyr. This implies that, unlike the LP or Shu models, we cannot estimate the age of the source based on its density profile alone.

In this study, we adopt a typical set of density profiles, averaged along the characteristic scale height, from one of the magnetic cycles predicted by the TM05 model. The density structure repeatedly goes through phase $\phi = 1$ to 15 in an evolution cycle, as shown by the solid curves in Figure 1. Here we only plot the more representative phases. The dotted curve in Figure 1 shows the initial density profile at the time hydrostatic equilibrium is established in the central region of the core ($t = 0$), which nearly follows a power-law relation of index -1.7. We can choose density profiles of any cycle for this study, as they are all similar. In other words, different cycles have the same predicted density profiles and quantitatively similar phases. The age of the chosen magnetic cycle is from $t = 33,750$ to 37,250 yr after the formation of the central hydrostatic core. By this time, the series of magnetic cycles has been well established.

The model cloud in TM05 has an equatorial radius of 4.23 pc. However, the thermally and magnetically supercritical fragment extends to approximately 9000 AU and contains $\sim 9\ M_{\odot}$. Outside this region, hardly any evolution takes place (see Fig. 1). In order to compare with observations, we truncate the density profiles at an outer radius within which the dynamical infall takes place. This is the "envelope," at the center of which the protostar is forming. By scaling the density profiles, the theoretical TM05 model is applied to observed objects of different masses. (This kind of scaling of the density profiles implies a corresponding scaling of the magnetic field profiles, but since no information on the magnetic field is available from observations, we do not discuss this implication further in this paper.)

Although the TM05 model has a flattened morphology (Fiedler & Mouschovias 1993), we only use a spherical density profile. The flattened molecular cloud has a radius of several pc, which is much larger than the scale studied here. LMW03 has tested geometric effects by elongating the envelope, and shown that flattening the envelope will artificially make a steeper flux density profile in *u-v* space. However, the analysis normalized the maximum flux density, which is different than the effect studied here. To better compare the effect a flattened envelope has on our modeling, we modified our spherical envelope model by multiplying the predicted image with a flat-shaped mask with exponentially decayed edges similar to a flattened envelope. The half-thickness of the "disk" is one-fifth of the radius, which gives a flattening ratio similar to that in the TM05 model. In this case, the observed flux density is less steep at small *u-v* distances, but is unchanged beyond *u-v* distances of 10 kλ. This is because fewer large-scale components, or small *u-v* distance components, contribute in the flattened structure than in a spherical model. We fit the simulated data of a flattened envelope with our spherical model and found that the spherical model fits the data very well with the same density profile, but that the mass is overestimated. In addition, the density profile from TM05 has been averaged along the characteristic scale height, which also helps mitigate the effect of a flattened envelope. On the other hand, the vertical density profile needs to be better modeled (see the observed flattened envelope in Looney et al. 2007), which is beyond the scope of this paper. Finally, a circumstellar disk may exist inside the envelope, and its emission is also taken into account in the model; this is described in more detail in § 3.4 and § 4.

3.2. *Grain Properties and Temperature Profiles*

Properties of dust grains, such as composition and size, determine their extinction and emission, as well as the temperature structure and the observable dust emission of the envelope. Here we adopt the grain model of Wolfire & Cassinelli (1986), in which the material mixture and size distributions of the Mathis-Rumpl-Nordsieck (MRN) model (Mathis et al. 1977) and optical constants of grains in Draine & Lee (1984) are used. The grain model consists a mixture of uncoated graphite and silicate with particle sizes ranging from 0.005 to 0.25 μm, and a power-law size distribution of index -3.5. It is important to note that the grains in TM05 are spherical and uniform in size, with a different chemical composition from those in the MRN model. However, these grain differences are not significant in the theoretical model evolution (Desch & Mouschovias 2001).

The mass opacity coefficient κ_ν of the grain is frequency dependent and typically follows a power-law relation $\kappa_\nu \propto \nu^\beta$. The index β varies with environment and is related to grain properties. At submillimeter wavelengths, the unevolved grains of the ISM have $\beta \approx 2$. However, in disks and dense cores β decreases to 1, mainly due to grain growth (e.g., Beckwith & Sargent 1991; Natta et al. 2007). Although our observations are only at a single wavelength, κ_ν of a wider range of frequency is still needed for computing a self-consistent temperature profile, since radiation of all frequencies contributes to the total luminosity. Our model uses the MRN grain model $\beta = 2$ at optical and infrared wavelengths but assumes $\beta = 1$ at long wavelengths, and adopts $\kappa_\nu = 0.009$ cm^2 g^{-1} at $\lambda = 2.7$ mm. The model also assumes that the dust grain properties are uniform and do not change with radius in the envelope.

Temperature profiles are then considered based on the model grain properties. The temperature profile can be simplified as a power law with radius if the dust envelope is optically thin and the dust opacity has a power-law frequency dependence ($\kappa_\nu \propto \nu^\beta$); then temperature $T \propto r^{-2/(4+\beta)}$, assuming the central protostar is the only heating source. In the case of $\beta = 1$, the temperature is $T \propto r^{-0.4}$. But in our model, the inner part becomes optically thick as the density increases near the center (LMW03), so we calculate a self-consistent temperature profile for each fitting using the code of Wolfire & Cassinelli (1986). The code takes the luminosity of the central object and solves the radiative transfer equation, including the effects of both emission and extinction by the dust grains in the envelope. At each shell of the envelope, the luminosity is conserved.

The self-consistent temperature profiles are important for calculating the emission, but they contradict the isothermal assumptions in theoretical models. However, until non-isothermal theoretical models are developed, this is the best compromise (see also LMW03).

3.3. *Interferometric Filtering*

Although we use the power of the interferometer to resolve out the large-scale features of the envelope, it is important to point out that there is remnant envelope emission even with high-resolution configurations (e.g., LMW00). There are a few reasons for this. First, the envelope emission is power-law-like (e.g., LMW03), so the expected interferometric response from a Gaussian (Wilner & Welch 1994) is not applicable. Second, the inner edge cutoff is abrupt, especially with the steep density profile. The abruptness causes ripples in *u-v* space that create power at long baselines. The important point here is that the ability to detect a disk in the presence of an envelope is not set by the formal noise level or Fourier components, but by the intrinsic ability to model the complexity of the envelope (inner cutoff, asymmetric structure, etc.) and the resolution of the observations compared to the disk size and the inner cutoff of the envelope. In other words, it is difficult to separate the youngest circumstellar disk from the inner circumstellar envelope; revealing the embedded circumstellar disk still requires an understanding of the inner envelope.

Only interferometric data are used in this study. Single-dish data can give an upper limit at zero spacings, but should not be included in the fitting. Single-dish observations detect not only the emission from the inner envelope, but also that from the outer part of a cloud that is not actively involved in the protostar-forming process. Using interferometry, only structures of size scale similar to or smaller than the collapsing envelope are detected and modeled. Hence, the mass and radius we infer in this paper are not the total mass or the overall size of the prestellar cores, but that of the inner envelope undergoing the collapse, observed at $\lambda = 2.7$ mm.

3.4. *Modeling Details*

The observational data we use are from LMW00. To compare the observations and the theoretical model, we analyze the data in *u-v* space, where the data are not affected by the CLEAN algorithm or *u-v* sampling. The interferometric data are binned in *u-v* annuli around the source locations from LMW00 and averaged vectorially. The resulting *u-v* amplitudes for each bin are shown by asterisks in Figure 2. The displayed error bars are statistical error bars based on the standard deviation of the mean of the data points in the bin with a minimum of 10%, reflecting the uncertainty in the overall calibration. In the cases where the binary systems were separated by more than 10″, the companion sources were subtracted out of the *u-v* data using the large-scale images of LMW00. The new *u-v* data were remapped to confirm that the large-scale emission from the companion sources was not

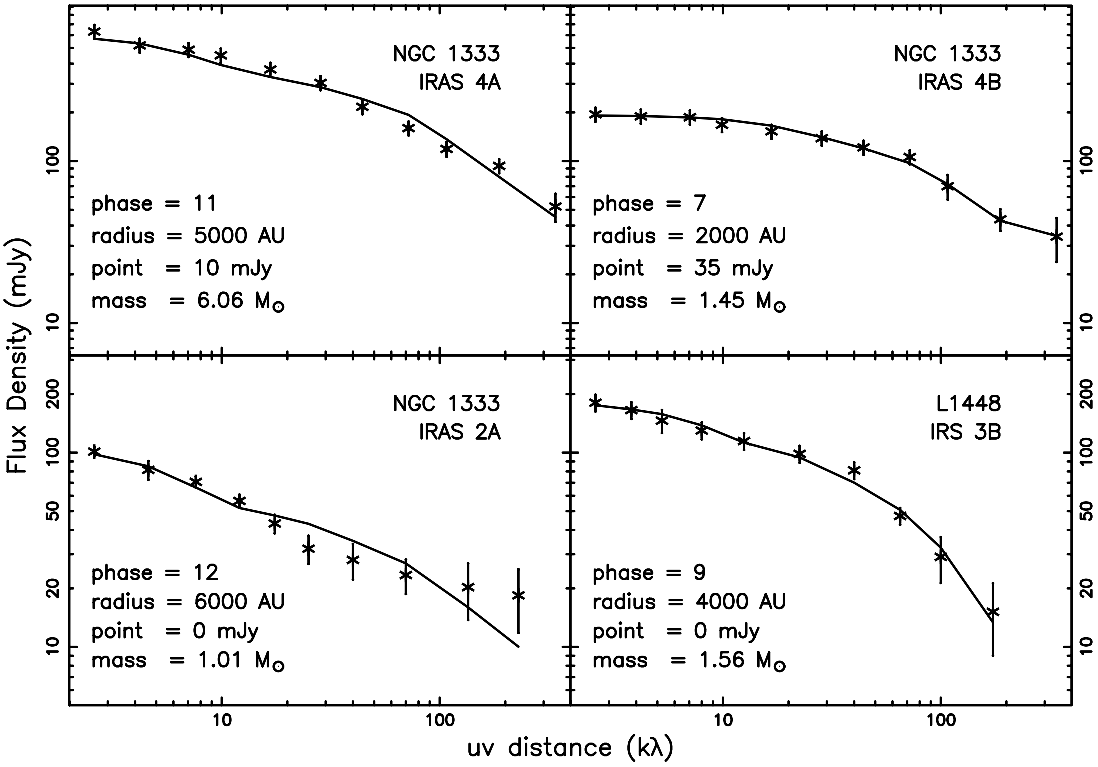

FIG. 2.—Flux density of the observational data and the best fit for each source with best-fit parameters listed. The χ^2 values are 1.49, 0.22, 1.30, and 0.41 for NGC 1333 IRAS 4A, IRAS 4B, IRAS 2A, and L1448 IRS 3B, respectively.

detected. Although there may exist some residual of small-scale emission from the companion envelope in the *u-v* data, vector averaging in *u-v* annuli will minimize its contribution.

The observational data shown in Figure 2 show the brightness distribution plotted at various antennas, or *u-v*, spacings, which is the Fourier transform of the sky brightness distribution. In other words, power at small *u-v* distance represents large-scale structures, and power at large *u-v* distance represents small-scale structures, i.e., a point source would be a constant at all antenna separations. The brightness distribution is determined by the circumstellar material surrounding the source, depending on density, temperature, and grain properties.

We model the circumstellar envelope emission as arising from a spherically symmetric dust envelope with TM05 radial density and self-consistent temperature profiles and an embedded circumstellar disk represented by an envelope-attenuated point source. The observed emission of most sources shows a circular symmetry and lack of significant internal structures (see images of the sources in LMW00). The combined radiative transfer code allows the calculation of the expected flux as a function of radius in the image plane or as a function of *u-v* distance in the Fourier plane. This provides the best way to trace emission structure to very small length scales, effectively the density and temperature profiles in the inner circumstellar envelope.

For each object, we did a parameter fitting of the model to the observational data with four degrees of freedom: evolutionary phase (density profiles) in the TM05 magnetic cycle, outer cutoff radius of the envelope, central point source flux, and envelope mass. The inner cutoff radius is fixed to be 10 AU to be consistent with the central sink approximation used in TM05, and the inner envelope is also truncated by the central disk physically. In Figure 3 we show the evolutionary phases in *u-v* space with all other parameters fixed for an example case of outer radius 5000 AU, envelope mass 5 $M_\odot$, no point source flux, and a fixed power-law temperature profile of index -0.4 and 500 K at 1 AU as an optically thin case (*the solid curves*). The difference between the phases in *u-v* space is mainly at large *u-v* spacings, corresponding to the shock propagation in the density profiles. On the other hand, adding a point source is like adding a constant in *u-v* space, which affects the slope in logarithmic plots; increasing the envelope mass increases the amplitude in all *u-v* spacings, especially in short *u-v* spacings; changing the outer radius alters the overall level and also the distribution of *u-v* amplitudes. The effects from varying each single parameter intertwine together, and degeneracy makes it difficult to point out which parameter is the key to each good fit; moreover, the self-consistent temperature profile considers the increase of optical depth near the center of the envelope and influences the predicted emission.

Model images of the envelope are computed with consideration of the envelope emission and the central point source attenuated by the dust envelope. The self-consistent temperature profiles are calculated from the assumed luminosity, which was derived from the far-infrared flux density (see LMW03) and is listed in column (2) in Table 1. The model images are multiplied by the observational primary beam, Fourier transformed into visibilities, and sampled with the same *u-v* coverage as the observations. Both model and observational data are binned and averaged in *u-v* annuli, shown as the flux density as a function of *u-v* spacing, and compared to each other. A reduced χ_r^2 is computed to determine the goodness of a fit. Among the four degrees of freedom, the total envelope mass is adjusted to minimize χ_r^2, while the other three parameters are fixed. This nonlinear minimization is done for any combination of these three parameters with outer radius ranging from 2000 to 9000 AU and point source flux as the ranges given in the parentheses in Table 1, and for each set of parameters a total envelope mass was obtained with

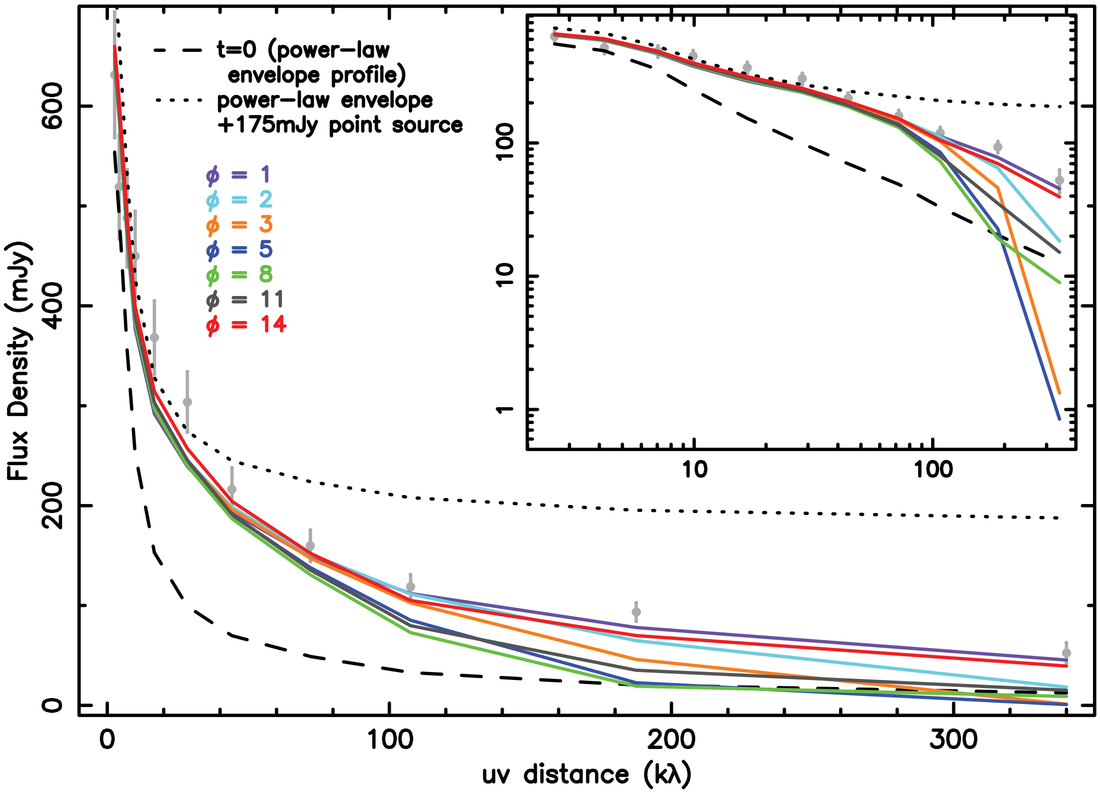

Fig. 3.—Solid curves show the example *u-v* visibilities from an optically thin envelope with outer radius 5000 AU, mass 5 $M_\odot$, and various evolutionary phases (no point source flux is added, and observational parameters such as the distance and *u-v* samplings are assumed to be the same as NGC 1333 IRAS 4A). Different colors correspond to different phases in the TM05 model, as the density profiles of these phases are plotted in Fig. 1. The dashed curve shows the flux density of the same case, but with the initial density profile of TM05, which is a nearly power-law profile with index −1.7. The dotted curve is the same nearly power-law envelope emission plus a constant 175 mJy (a point source flux), representing an unresolved disk. The same visibilities are also plotted in a logarithmic scale in the inset panel. The observational data points of NGC 1333 IRAS 4A are shown for comparison. The power-law envelope itself (*dashed curve*) is not a good fit; also, just adding a point source flux to the power-law density profile cannot fit the data (*dotted curve*). This is similar to the results from Jørgensen et al. (2005). However, the predicted envelope emission from the TM05 model is very different and a better fit to the data.

local minimal χ_r^2. Collecting the results of sets of parameters, the best fit, with global minimal χ_r^2 is found.

4. RESULTS AND DISCUSSION

In Figure 2, data are binned, averaged, and shown by asterisks with associated error bars, and the curves show the best fit for each source as a function of *u-v* distance, with the best-fit parameters given on the plot. The best-fit parameters do not need to be the same as those in LMW03, since a different theoretical model is used here. Figure 4 shows the corresponding density and temperature profiles for these best fits. The straight dashed lines in the temperature plots are lines with slope −0.4, which would be the temperature profiles if the envelopes are optically thin ($T \propto r^{-0.4}$). We can see that the outer part of the envelopes is nearly optically thin, and becomes hotter and optically thicker at smaller radii.

We refer to a fit with more than 90% confidence level as an acceptable fit, and a summary of acceptable fits is given in Table 1. Fitting with density profiles at different phases implies that the systems may be at different phases of a magnetic cycle. Presumably, if we had data for more objects we might catch systems at all phases. The acceptable fits spread over a range of parameters depending on the signal-to-noise ratio of the observations. One important aspect of the modeling is the clear need for high signal-to-noise ratio data. The χ^2 value is the evaluation quantity

TABLE 1

Acceptable Fits

Source Name	Luminosity[a] ($L_\odot$)	Density Profiles[b] (Phase)	Outer Radius (AU)	Point Source Flux[c] (mJy)	Envelope Mass ($M_\odot$)	Good Fits[d]
NGC 1333 IRAS 4A	16	9–11	4000–5000	0–50 (0–50)	4.88–6.23	15/720
NGC 1333 IRAS 4B	5.2	1–14	2000–6000	0–56 (0–56)	1.45–4.02	302/1215
NGC 1333 IRAS 2A	30	2–13	5000–8000	0–7 (0–21)	0.76–1.37	49/480
L1448 IRS 3B	6.8	3–12	2000–9000	0–18 (0–18)	0.75–4.37	223/480

Notes.—A set of parameters gives a good fit (a so-called acceptable fit) if the reduced χ^2 is within the 90% confidence level. For each parameter the range of acceptable fits is given.

[a] All sources here are binary systems and flux of single component is assumed based on the ratio of fluxes at $\lambda = 2.7$ mm (see LMW03).

[b] The number corresponds to a specific phase in the cycle for which the density profile of the TM05 model provides an acceptable fit (see Fig. 1).

[c] The parameter search ranges while fitting are listed in the parentheses.

[d] The number of good fits and the total number of combinations while fitting.

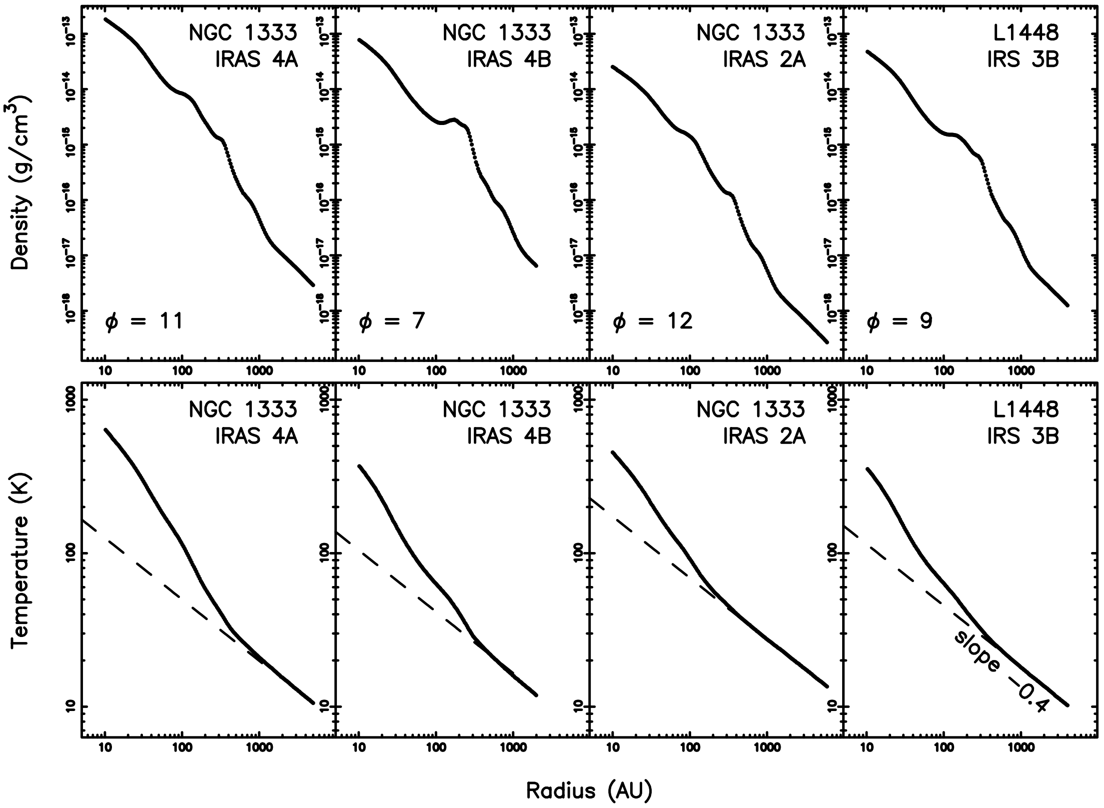

FIG. 4.—Density and temperature profiles of the best fit for each source. The straight dashed lines in the temperature plots show the optically thin case.

of the goodness of a set of parameters, and is smaller when the observational uncertainties are larger; low signal-to-noise ratio data make acceptable fits easier. When the signal-to-noise ratio is too low, the fitting becomes meaningless, which is why we apply the analysis only to four sources from LMW00. This argument is consistent with our results that the best constraints of model parameters is provided by the highest signal-to-noise observation IRAS 4A among all four sources. Given better signal-to-noise ratio data at more wavelengths, in the future we may be able to constrain the model better not only for more sources but also for better-constrained parameters.

Nonetheless, the most important result of this study is that with the TM05 theoretical model, we can easily fit the observations of these sources without conflicts of ages, unlike the fits using the LP or Shu models (LMW03), although the exact source age is not determinable by comparison with the TM05 model. Due to the episodic nature of the theoretical model, we are not fitting nor implying a specific age for the source, but the range of age is 15–255 kyr. Parsec-scale jets and outflows have been found in these regions and can be used to estimate the ages of central sources that drive the outflows. For example, the timescale of the outflows in NGC 1333 is of order 10^5 yr (Bally et al. 1996), which is consistent with the age range of the TM05 model.

We use the phases of a typical magnetic cycle for the fitting. TM05b's Figure 5 shows the beginning evolution after the central sink is introduced and the system has the first magnetic cycle at about $t = 15$ kyr; then it repeats the magnetic cycles as in TM05b's Figures 8 and 9 until $t = 255$ kyr, when the sink mass reaches 1 $M_\odot$ and the simulation stops. Once the cycling behavior has been well established, all physical quantities show high similarity of variation from cycle to cycle. Only the period of a cycle, which is about several thousand years, decreases with time, controlled by the ambipolar-diffusion timescale at the position of the magnetic wall; other than that, there is no obvious difference between cycles. So given a fit to a density profile, the system may be at a specific phase of any cycle during this epoch. However, the age range suggested by the theoretical model is consistent with the age estimated by the outflows' scale, which implies that the observational data are consistent with the TM05 picture of early star formation.

One of the most important differences between the TM05 and the Shu or LP models is that the steep power-law-like density profiles of TM05 are actually not in equilibrium, while $\rho \propto r^{-2}$ in the other models, corresponding to the singular isothermal sphere, is a critical equilibrium situation. In the Shu or LP models, the collapse is induced by an outward-moving rarefaction wave, and the density changes dramatically after being affected by the wave; in TM05, the system is collapsing and mass keeps accreting onto the central protostar dynamically without making an abrupt change, except for the relatively small bump generated by the magnetic wall. Periodic creation and dispersion of the magnetic wall dominate the variation of density profiles and also the accretion, so the whole collapse process is regulated by magnetic forces. Accounting for magnetic fields in the theoretical models, the density profiles at later times of the evolution are very different from those of the Shu or LP models, and are better matched with the observations and estimated ages from outflows.

Can we constrain the earliest disks? Table 1 shows that in all cases, we can fit our sources without a circumstellar disk component at the 90% confidence level. On the other hand, a disk is expected early on in the collapse process due to the rotation and/or magnetic fields in the initial cloud. As material accretes, the disk receives more mass from the envelope. The mass is processed in the disk, which regulates mass flow through the disk and onto the protostar. The magnetic fields within the disk and star give rise to an outflow (e.g., Shang et al. 2007; Pudritz et al. 2007) that is typically seen even in very young sources, suggesting that a disk is established nearly concurrently with the protostar's growth in luminosity as it collapses to stellar size. In fact, simple theoretical arguments suggest that the disk evolves early and grows quickly with time as $\sim t^2$ or $\sim t^3$ (e.g., Stahler & Palla 2005), which depends crucially on the mass accretion rate.

Although not a statistical requirement, we do expect these sources to have some sort of deeply embedded circumstellar disks in the center of the infalling envelopes. We can use HL Tau, which was modeled in Mundy et al. (1996) as a standard candle to estimate the mass of the disks in our modeled systems. Also using BIMA $\lambda = 2.7$ mm dust continuum observations, the total flux from HL Tau was $\sim$100 mJy, and the derived disk mass from modeling was $\sim 0.05\ M_\odot$. Based on the assumption of equal flux to disk mass ratio corrected by the distance, the value 0.010 Jy in the best-fit point-source flux for NGC 1333 IRAS 4A corresponds to a disk of mass 0.03 $M_\odot$, and 0.035 Jy for IRAS 4B corresponds to a 0.11 $M_\odot$ disk. A distance to NGC 1333 of 350 pc has been assumed here. If we use a distance of 250 pc instead, the estimated mass of embedded disks for the best fits would be 0.016 and 0.056 $M_\odot$ for IRAS 4A and IRAS 4B, respectively. The acceptable fits with maximum disk components give disk mass of 0.16, 0.18, 0.065, and 0.041 $M_\odot$ for NGC 1333 IRAS 4A, IRAS 4B, IRAS 2A, and L1448 IRS 3B, respectively. It gives an upper limit of disk mass to IRAS 2A, since model parameters with higher point source flux cannot fit anymore.

Unlike in Jørgensen et al. (2005), a disk component is not crucially necessary in our modeling. The major reason is that different envelope models are used. TM05 predict a very different visibility amplitude profile from what is expected by a power-law density profile. For example, in Figure 3, the dashed curve is the predicted *u-v* amplitude of a nearly power-law density profile of index -1.7 (the initial density profile in the TM05 simulation), and the dotted curve is generated with the same density profile, but with a point-source flux representing an unresolved circumstellar disk. As can be seen, the envelope emission from a power-law density profile shows a very different shape than from predicted by the phases of the magnetic cycle. TM05 density profiles are able to fit the data well without adding a Gaussian disk (cf. Jørgensen et al. 2005). Again, this shows the importance of understanding the collapsing envelope in order to understand the embedded disk.

5. SUMMARY

1. Although interferometry is a powerful tool in resolving out the large-scale emission of the envelope, the ability to detect a disk in the presence of an envelope is not set by the formal noise level or Fourier components, but by the intrinsic ability to model the complexity of the envelope (inner cutoff, asymmetric structure, etc.) and by the resolution of the observations compared to the disk size and the inner cutoff of the envelope. In other words, reliable detection of the embedded circumstellar disk requires a knowledge of the physical parameters of the inner envelope.

2. Our observational data are consistent with the theoretical predictions of TM05 concerning the density profiles. Moreover, there is no discrepancy in age based on the size of the outflows, unlike the fitting results of the simpler Shu or LP solutions to the isothermal sphere (e.g., LMW03). It is important to note that the exact age cannot be determined by comparison of the data with the TM05 model due to its periodic nature. Regardless of the collapse initiation, the magnetic fields may play an important role early on in the collapse process. To expand this comparison, we will continue to observe Class 0 objects at higher sensitivity and multiple wavelengths, better incorporating the theoretical models into our comparisons.

3. Although our initial results do not require the existence of circumstellar disks (acceptable fits of 0.0–0.11 $M_\odot$), we can place upper limits on the disk masses. In general, the disks are less massive than $\sim 0.1\ M_\odot$. The youngest circumstellar disk mass is not overly massive compared to other well known Class II or III circumstellar disks. The fact that a disk component is not statistically necessary in this modeling is different from similar work at submillimeter wavelengths by Jørgensen et al. (2005). The main reason is that different visibility profiles are predicted by TM05 than for envelopes of power-law density.

H. F. C. and L. W. L. acknowledge support from the Laboratory for Astronomical Imaging at the University of Illinois and the NSF under grant AST-05-40459 and NASA Origins grant NNG06GE41G. K. T. acknowledges support by NSF grants AST-02-06216 and AST-02-39759, by the NASA Theoretical Astrophysics Program grant NNG04G178G, and by the Kavli Institute for Cosmological Physics at the University of Chicago through NSF grants PHY-01-14422 and PHY-05-51142 and an endowment from the Kavli Foundation and its founder Fred Kavli. L. G. M. acknowledges NSF grant AST-05-40450 and NASA Origins grant NNG06GE16G. H. F. C., L. W. L., and T. M. acknowledge support from the NSF under grant AST-07-09206. Helpful comments by an anonymous referee are gratefully acknowledged.

REFERENCES

Adams, F. C., Lada, C. J., & Shu, F. H. 1987, ApJ, 312, 788

Andre, P., Ward-Thompson, D., & Barsony, M. 1993, ApJ, 406, 122

———. 2000, in Protostars and Planets IV, ed. V. Mannings, A. Boss, & S. S. Russell (Tucson: Univ. Arizona Press), 59

Andrews, S. M., & Williams, J. P. 2005, ApJ, 631, 1134

Arce, H. G., & Sargent, A. I. 2006, ApJ, 646, 1070

Bachiller, R. 1996, ARA&A, 34, 111

Bally, J., Devine, D., & Reipurth, B. 1996, ApJ, 473, L49

Barranco, J. A., & Goodman, A. A. 1998, ApJ, 504, 207

Beckwith, S. V. W., & Sargent, A. I. 1991, ApJ, 381, 250

Benson, P. J., & Myers, P. C. 1989, ApJS, 71, 89

Blake, G. A., Sandell, G., van Dishoeck, E. F., Groesbeck, T. D., Mundy, L. G., & Aspin, C. 1995, ApJ, 441, 689

Brinch, C., Crapsi, A., Jørgensen, J. K., Hogerheijde, M. R., & Hill, T. 2007, A&A, 475, 915

Cernis, K. 1990, Ap&SS, 166, 315

———. 1993, Baltic Astron., 2, 214

Choi, M. 2001, ApJ, 553, 219

———. 2005, ApJ, 630, 976

de Zeeuw, P. T., Hoogerwerf, R., de Bruijne, J. H. J., Brown, A. G. A., & Blaauw, A. 1999, AJ, 117, 354

Desch, S. J., & Mouschovias, T. Ch. 2001, ApJ, 550, 314

Di Francesco, J., Myers, P. C., Wilner, D. J., Ohashi, N., & Mardones, D. 2001, ApJ, 562, 770

Draine, B. T., & Lee, H. M. 1984, ApJ, 285, 89

Elmegreen, B. G., & Scalo, J. 2004, ARA&A, 42, 211

Enoch, M. L., et al. 2006, ApJ, 638, 293

Fiedler, R. A., & Mouschovias, T. Ch. 1993, ApJ, 415, 680

Girart, J. M., Rao, R., & Marrone, D. P. 2006, Science, 313, 812

Harvey, D. W. A., Wilner, D. J., Myers, P. C., Tafalla, M., & Mardones, D. 2003, ApJ, 583, 809

Hunter, C. 1977, ApJ, 218, 834

Jørgensen, J. K., Bourke, T. L., Myers, P. C., Schöier, F. L., van Dishoeck, E. F., & Wilner, D. J. 2005, ApJ, 632, 973

Jørgensen, J. K., Hogerheijde, M. R., van Dishoeck, E. F., Blake, G. A., & Schöier, F. L. 2004, A&A, 413, 993

Jørgensen, J. K., et al. 2006, ApJ, 645, 1246

Keene, J., & Masson, C. R. 1990, ApJ, 355, 635

Kirk, H., Johnstone, D., & Tafalla, M. 2007, ApJ, 668, 1042

Knee, L. B. G., & Sandell, G. 2000, A&A, 361, 671

Kwon, W., Looney, L. W., Crutcher, R. M., & Kirk, J. M. 2006, ApJ, 653, 1358

Lada, C. J., Alves, J., & Lada, E. A. 1996, AJ, 111, 1964

Lada, C. J., & Wilking, B. A. 1984, ApJ, 287, 610

Larson, R. B. 1969, MNRAS, 145, 271

Lay, O. P., Carlstrom, J. E., & Hills, R. E. 1995, ApJ, 452, L73

Looney, L. W., Mundy, L. G., & Welch, W. J. 2000, ApJ, 529, 477 (LMW00)

———. 2003, ApJ, 592, 255 (LMW03)

Looney, L. W., Tobin, J. J., & Kwon, W. 2007, ApJ, 670, L131

Mac Low, M.-M., & Klessen, R. S. 2004, Rev. Mod. Phys., 76, 125

Mathis, J. S., Rumpl, W., & Nordsieck, K. H. 1977, ApJ, 217, 425

Mouschovias, T. Ch. 1996, in The Role of Dust in the Formation of Stars, ed. H. U. Käufl & R. Siebenmorgen (Berlin: Springer), 382

Mouschovias, T. Ch., & Ciolek, G. E. 1999, in The Origin of Stars and Planetary Systems, ed. C. J. Lada & N. D. Kylafis (Dordrecht: Kluwer), 305

Mundy, L. G., et al. 1996, ApJ, 464, L169

Natta, A., Testi, L., Calvet, N., Henning, T., Waters, R., & Wilner, D. 2007, in Protostars and Planets V, ed. B. Reipurth, D. Jewitt, & K. Keil (Tucson: Univ. Arizona Press), 767

O’Linger, J. C., Cole, D. M., Ressler, M. E., & Wolf-Chase, G. 2006, AJ, 131, 2601

Penston, M. V. 1969, MNRAS, 144, 425

Pudritz, R. E., Ouyed, R., Fendt, C., & Brandenburg, A. 2007, in Protostars and Planets V, ed. B. Reipurth, D. Jewitt, & K. Keil (Tucson: Univ. Arizona Press), 277

Sandell, G., & Knee, L. B. G. 2001, ApJ, 546, L49

Seale, J. P., & Looney, L. W. 2008, ApJ, 675, 427

Shang, H., Li, Z.-Y., & Hirano, N. 2007, in Protostars and Planets V, ed. B. Reipurth, D. Jewitt, & K. Keil (Tucson: Univ. Arizona Press), 261

Shu, F. H. 1977, ApJ, 214, 488

Stahler, S. W., & Palla, F. 2005, The Formation of Stars (Weinheim: Wiley-VCH)

Tassis, K., & Mouschovias, T. Ch. 2005a, ApJ, 618, 769 (TM05a)

———. 2005b, ApJ, 618, 783 (TM05b)

———. 2007a, ApJ, 660, 370

———. 2007b, ApJ, 660, 388

———. 2007c, ApJ, 660, 402

Tobin, J. J., Looney, L. W., Mundy, L. G., Kwon, W., & Hamidouche, M. 2007, ApJ, 659, 1404

Whitworth, A., & Summers, D. 1985, MNRAS, 214, 1

Wilking, B. A., Meyer, M. R., Greene, T. P., Mikhail, A., & Carlson, G. 2004, AJ, 127, 1131

Wilner, D. J., & Welch, W. J. 1994, ApJ, 427, 898

Wolf-Chase, G. A., Barsony, M., & O’Linger, J. 2000, AJ, 120, 1467

Wolfire, M. G., & Cassinelli, J. P. 1986, ApJ, 310, 207